

Thermohydraulic performance and correlation development for solar air heater having rough absorber surface using chamfered-square elements

Man Singh Azad

CSIR-Central Mechanical Engineering Research Institute, Mahatma Gandhi Avenue, Durgapur, West Bengal, 713209, India.

ARTICLE INFO

Received: 26 Dec. 2021;
Received in revised form:
06 June 2022;
Accepted: 12 June 2022;
Published online:
24 June 2022

Keywords:

CFD
Correlation
Overall Enhancement Ratio,
Thermohydraulic Performance
Solar Air Heater

ABSTRACT

A very simple and economical device used for harnessing freely available energy from sun is solar air heater. But these solar air heaters are inefficient due to the low co-efficient of heat of air. Making artificially rough absorber plate is very common amongst the various techniques applied on solar air heater to enhance the performance. Square elements cut diagonally and glued on the absorber surface to generate the roughness. The impact of roughness parameters such Relative roughness height (RRH) of 0.44 to 0.077, Relative roughness pitch(RRP) of 3 to 9 and square element arm length (ALSE) of 4 mm to 10 mm on the performance of an artificially roughened solar air heater has been numerically explored. The Reynolds number of the absorber plate was adjusted from 4250 to 20000, but the heat flux remained constant at 1000 W/m². The flow turbulence was handled using the “ANSYS FLUENT software's renormalized group (RNG) k-ε with enhanced wall treatment” turbulence model. In terms of Nusselt number and friction factor, the effects of roughness parameters such as RRP, RRH, and ALSE on the performance of artificially roughened solar air heaters have been explored. To test their increased efficiency, Nusselt number and friction factor of roughened solar air heaters (SAH) has been compared at similar flow conditions with plain one.

© Published at www.ijtf.org

1. Introduction

Energy demand is increasing in lockstep with population growth, industrialisation, and transportation. The unrestricted use of the earth's finite reserves of fossil fuels has resulted in not just energy depletion on a global scale, but also a severe problem of environmental deterioration. As a result, the scientific community had to reevaluate and

come up with new strategies to meet future energy demands. One of the most abundant renewable energy sources is solar energy which has the ability to hold down future rising energy demands. The SAH absorbs the sun's rays and transfers the heat to the air blowing beneath it. There are numerous applications for hot air such as food processing, wood seasoning, space heating etc.

*Corresponding e-mail: msazada@gmail.com (Man Singh Azad)

The thermal efficiency of a SAH is poor due to the low co-efficient of heat of air, as the heat transfer between the heated absorber plate and passing air is minimal even for turbulent flow[1].

Various researchers have utilised a variety of approaches to improve the heat transfer rate and enhance the SAH's thermal efficiency. Various types of Fins [2-5], packed bed [6] and intentionally roughened absorber plate [7-9] were among the first approaches used. Artificially applying roughness over absorber surface of any SAH is the simplest, most cost-effective, and widely recognised of all the ways.

The growth of a laminar sub-layer over a typical absorber plate acts as a thermal barrier to heat transfer, resulting in poor performance from SAH.

Convective heat transfer is improved by introducing an artificial roughness element into the flow. However, because friction losses increase, more power is required to drive the blower and keep the air flowing through the duct.

Many researchers have studied the efficacy of SAHs with variety of roughness provided artificially and grouped in various ways.

Kumar et al. [7] examined the impact of roughness factors in depth. Vyas and Shringi [10] analyzed the efficiency of a SAH that had been artificially roughened with baffles and discovered that it was 2.23 times more efficient than a smooth one.

The performance of SAH employing tiny diameter wire as a roughness element was studied experimentally by Prasad and Saini [11] and reported a significant increase in Nusselt number and friction factor.

V-continuous rib, V-discrete rib, 60° ribs and 45° ribs roughness elements were studied experimentally by Karwa et al. [12]. They discovered that discrete ribs and 60° ribs outperformed continuous rib and 45° ribs respectively.

A SAH having double-pass channels with varied rib shapes roughness was tested by Rasool et al. [13] numerically and Boot-shaped ribs outperformed house-shaped and traditional square-shaped ribs. Tapas et al. [14] evaluated numerically the performance of SAH roughened artificially by circular transverse wire rib and discovered considerable heat transfer augmentation.

The majority of the efforts done are experimental, according to the literature. As a result, a numerical analysis may be successfully carried out as an alternative to costly experimental examination in a short period of time to study different orientations and their effectiveness to enhancement of thermohydraulic efficiency of solar air heaters.

It's a unique design to use diagonally chamfered square elements to create roughness on absorber surface of SAH. To explore the impact of roughness characteristics on SAH efficiency, a CFD based numerical analysis is presented.

Nomenclature			
Length of duct in millimeters	L	Reynolds number	Re
Height of duct in millimeters	H	Relative roughness pitch	P/e
Width of duct in millimeters	W	Nusselt number for smooth duct	Nu _s
Aspect ratio of duct	W/H	Nusselt number for roughened duct	Nu _r
Hydraulic diameter of duct in millimeters	D	Friction factor for smooth duct	f _s
Height of roughness element in millimeters	e	Friction factor for roughened duct	f _r
length of arm of square element in millimeters	A	Heat flux in W/m ²	I
Relative roughness height	e/D		

2. Roughness Material and Used Method

The roughness element was made of aluminum same as that of absorber plate and pasted inside of the plate. It was square

elements chamfered diagonally and arm length varied from 4 mm to 10 mm whereas height was varied from 2 to 3.5 mm.

The SAH employed for investigation had a hydraulic diameter (D) of 45 mm. For all of the studies, an evenly distributed heat flux of 1000W/m² was delivered over SAH's absorber plate. The Reynolds number range applied in this investigation was 4250 - 20000 to evaluate the effect of SAH roughness on Nusselt number and friction factor.

Fig. 2 shows a schematic representation of the roughness used in this investigation. Only the absorber plate had roughness, whereas the remaining walls of the test section were kept smooth. The length (L), width (W) and height (H) of the solar air heater employed for CFD analysis were 2100mm, 200mm, and 25mm, respectively (H). Throughout the study, the aspect ratio, which is the ratio of width to height, was set to 8. The flow domain is comprises into three sections: entry, test, and exit. The entry and exit sections were made suitably large to minimize the end consequences. A three-dimensional flow domain was chosen for this study, assuming secondary flow occurred due to sloped roughness geometry in the route of air flow.

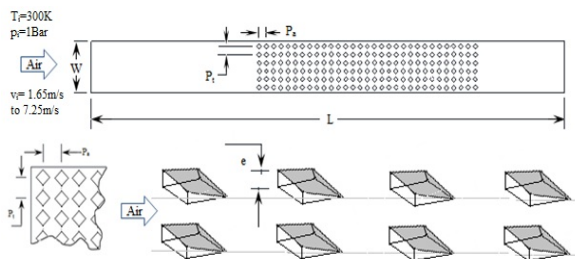


Fig. 1. Schematic diagram of the studied roughness.

ANSYS 16.0's ICEM CFD was used to mesh the three-dimensional flow domains explored in this work [15]. In comparison to other regions, a finer mesh was produced in the rib region to evaluate flow dynamics and heat transmission properly.

The governing equations for the Three-Dimensional domain are presented below as:

Equation of Continuity [15]:

$$\frac{\partial u}{\partial x} + \frac{\partial v}{\partial y} + \frac{\partial w}{\partial z} = 0 \quad \dots (1)$$

Equation of momentum [15]:

$$u \frac{\partial u}{\partial x} + v \frac{\partial u}{\partial y} + w \frac{\partial u}{\partial z} = -\frac{1}{\rho} \frac{\partial p}{\partial x} + \nu \left(\frac{\partial^2 u}{\partial x^2} + \frac{\partial^2 u}{\partial y^2} + \frac{\partial^2 u}{\partial z^2} \right) \quad \dots (2)$$

$$u \frac{\partial v}{\partial x} + v \frac{\partial v}{\partial y} + w \frac{\partial v}{\partial z} = -\frac{1}{\rho} \frac{\partial p}{\partial y} + \nu \left(\frac{\partial^2 v}{\partial x^2} + \frac{\partial^2 v}{\partial y^2} + \frac{\partial^2 v}{\partial z^2} \right) + g\beta(T - T_\infty) \quad \dots (3)$$

$$u \frac{\partial w}{\partial x} + v \frac{\partial w}{\partial y} + w \frac{\partial w}{\partial z} = -\frac{1}{\rho} \frac{\partial p}{\partial z} + \nu \left(\frac{\partial^2 w}{\partial x^2} + \frac{\partial^2 w}{\partial y^2} + \frac{\partial^2 w}{\partial z^2} \right) \quad \dots (4)$$

Energy equation [15]:

$$u \frac{\partial T}{\partial x} + v \frac{\partial T}{\partial y} + w \frac{\partial T}{\partial z} = \alpha \left(\frac{\partial^2 T}{\partial x^2} + \frac{\partial^2 T}{\partial y^2} + \frac{\partial^2 T}{\partial z^2} \right) \quad \dots (5)$$

where the components of fluid velocity in the x, y, and z directions are u,v, and w, respectively.

p=Pressure,

T = Temperature

T_∞ = Ambient temperature.

In this study, ANSYS fluent 16.0 was utilised as computational tool for the computational analysis. This research took into account fully matured, steady state, and turbulent flow. Except for the absorber plate, all of the walls of the solar air heater duct were considered to be adiabatic. Throughout all of the testing, the air was working fluid and considered incompressible. All of the following assumptions were based on the results of prior tests conducted by the various investigators [15].

Table 1

Thermophysical properties [15]

Parameter	Symbol	Unit	Air	Absorber plate (Al)
Specific heat	C_p	J/kgK	1004.9	871.00
Thermal conductivity	k	W/mK	0.02624	202.40
Density	ρ	kg/m ³	1.225	2719.00
Viscosity	μ	N/m ²	1.846	-
		$\times 10^5$		
Thermal expansion coefficient	β	K ⁻¹	0.0034	-

The velocity inflow at inlet and outflow at outlet were defined as the solution domain and boundary conditions. Domain turbulence was defined using the turbulence intensity and hydraulic diameter. Steady and uniformly distributed heat flux was applied on absorber plate as boundary condition. For the pressure-velocity coupling in this computational investigation, the second order upwind numerical scheme ‘‘SIMPLE (semi-implicit technique for pressure linked equations) algorithm’’ was used [15].

3. Model Selection and Validation

The selection and validation of the best suited turbulence model is a critical stage in any computational analysis because the outcome is dependent on the model used. The Dittus-Boelter empirical correlation and modified Blasius equation were compared for smooth ducts with the same cross section for Nusselt number and friction, respectively, to validate and select the best among different turbulence models i.e. Standard (STD) k-ε model, Renormalized group (RNG) k-ε model, and Realizable (RLG) k-ε model [15].

Dittus-Boelter empirical correlation

$$Nu = 0.024 Re^{0.8} Pr^{0.4} \quad (6)$$

Modified Blasius equation

$$f = 0.085 Re^{-0.25} \quad (7)$$

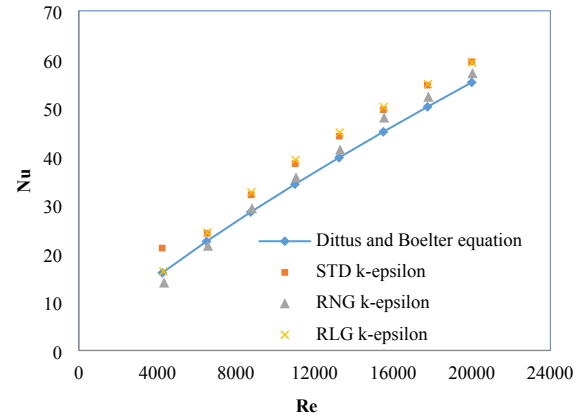


Fig. 2. Comparison of various anticipated turbulence models and Dittus-Boelter correlations.

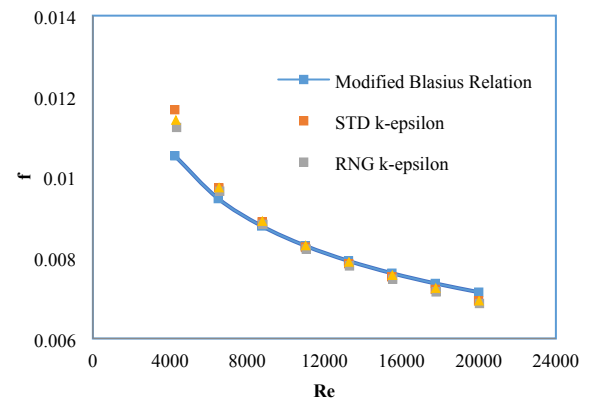


Fig. 3. Comparison of various anticipated turbulence models and Modified Blasius relation.

The best suited turbulence model found and selected is Realizable (RLG) k-ε model. The questions solved in Ansys fluent are as follows for the selected turbulence model:-

$$\frac{\partial}{\partial t}(pk) + \frac{\partial}{\partial x_j}(pk u_j) = \frac{\partial}{\partial x_j} \left[\left(\mu + \frac{\mu_t}{\sigma_k} \right) \frac{\partial k}{\partial x_j} \right] + G_k + G_b - \rho \varepsilon - Y_M + S_k \quad (8)$$

$$\frac{\partial}{\partial t}(p\varepsilon) + \frac{\partial}{\partial x_j}(p\varepsilon u_j) = \frac{\partial}{\partial x_j} \left[\left(\mu + \frac{\mu_t}{\sigma_\varepsilon} \right) \frac{\partial \varepsilon}{\partial x_j} \right] + \rho C_{1\varepsilon} S_\varepsilon - \rho C_{2\varepsilon} \frac{\varepsilon^2}{k + \sqrt{v\varepsilon}} + C_{1\varepsilon k} \frac{\varepsilon}{k} C_{3\varepsilon} G_b + S_\varepsilon \quad (9)$$

where;

$$C_1 = \max \left[0.43, \frac{\eta}{\eta + 5} \right], \quad \eta = S_\varepsilon^k, \quad S = \sqrt{2S_{ij}S_{ij}}$$

In these equations, G_k represents the generation of turbulence kinetic energy due to the mean velocity gradients, G_b is the

generation of turbulence kinetic energy due to buoyancy, Y_M represents the contribution of the fluctuating dilatation in compressible turbulence to the overall dissipation rate. C_1 and C_2 are constants.

σ_k and σ_ϵ are the turbulent Prandtl numbers for k and ϵ respectively. S_k and S_ϵ are user-defined source terms.

4. Discussion and Conclusions

For both the roughened and smooth absorber plates, all simulation results are provided and contrasted. The rise in thermohydraulic efficiency of SAH at various flow rates is addressed below.

4.1 Characteristics of Heat Transfer

Providing artificial roughness over absorber plate causes turbulence in the laminar sub-layer area, which aids in improving the absorber plate's heat transfer rate. The roughness element's shape, size, direction, and pattern have a substantial impact on turbulence intensity and Nusselt number. The impacts of roughness factors such as RRH (e/D), RRP (P/e), and ALSE (A) on heat transfer and friction factor were investigated in this study. To imitate solar energy, a continuous and uniformly distributed heat flux of 1000 W/m² was applied on absorber plate. Range of Reynolds number used was 4250 to 20000.

4.1.1 Impact of Relative Roughness Height

For various levels of RRH (e/D) and fixed levels of RRP (P/e) of 6 and ALSE (A) of 6, Fig. 4 shows the variations in Nusselt number (Nu) as Reynolds number (Re) increases. At constant value of e/D, Nusselt number increases monotonically with increasing Reynolds number for fixed value of e/D. The reason for this is that when the Reynolds number rises, the turbulence intensity and turbulence dissipation rate rise, increasing the heat transfer rate. It's also evident that the Nusselt number rises with respect to rise in relative roughness height. As the relative roughness height rises, the roughness splays more into core flow, enhancing turbulence and the Nusselt number.

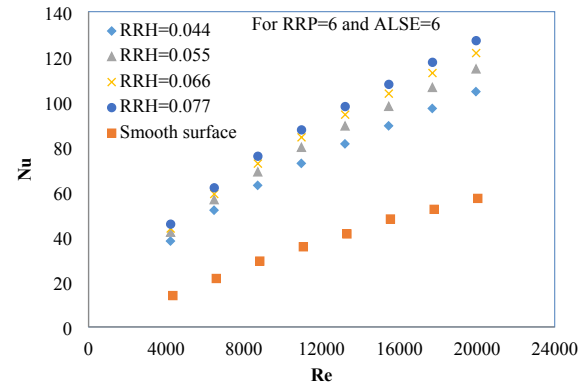


Fig. 4. Change in Nu against Re for different values of RRH (e/D) and a constant value of RRP (P/e) = 6, ALSE (A) = 6.

The Nusselt number rises with increase in RRH (e/D), as shown in the Fig. above. It is also obvious that putting artificial roughness on the absorber plate increases the heat transfer rate due to flow dissociation and reattachment of the free shear layer in between two ribs, which destroys the creation of the laminar sub-layer. Fig. 5 was created using the data in Fig. 4 to study the change in Nusselt number with increasing RRH versus Reynolds number values while keeping the other parameter values constant.

It can be seen in Fig. 5, increasing the RRH (e/D) increases the Nusselt number (Nu), reaching a maximum value of Nusselt number corresponding to a RRH of 0.077. More turbulence is produced when the RRH is increased, which improves the Nusselt number. Table 3 demonstrates the changes in Nusselt number w.r.t RRH.

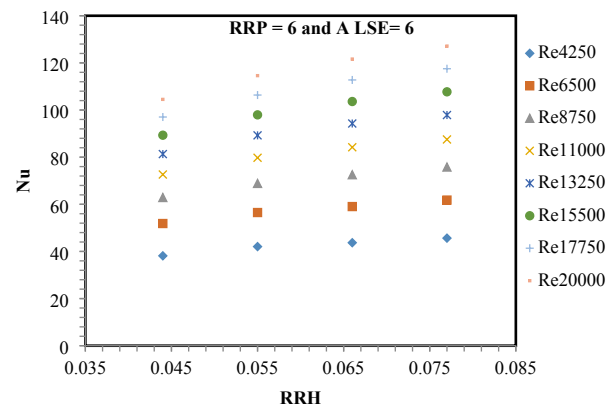


Fig. 5. Changes in Nu against RRH (e/D) and constant values of RRP = 6, ALSE = 6.

Table 2

Change in Nu against RRH

Constant roughness parameters	Change in RRH (e/D)	Change in Nusselt number (Nu) (%)
RRP = 6	0.044-	8.99-10.26
ALSE =6	0.055-	3.91-6.14
	0.066	
	0.066-	3.80-4.66
	0.077	

4.1.2 Effect of Relative roughness pitch (RRP)

Fig. 6 depicts the change in Nusselt number (Nu) when Reynolds number (Re) increases for various values of RRP (P/e) and constant values of RRH (e/D) of 0.077 and ALSE (A) of 6. The graphic shows that for a constant value of RRP, Nusselt number increases monotonically with Reynolds number. It can be seen that as the RRP (P/e) increases, Nusselt number falls. Fig. 6 shows that for each set of parameters, the highest Nusselt number is obtained at the lowest RRP.

Fig. 7 was created using the data in Fig.6 to look at how the Nusselt number changes when the RRP increases for different Reynolds numbers. Fig. 7 shows that Nusselt number reduces as RRP increases, with the maximum value of Nusselt number corresponding to RRP value of 5, which is the smallest RRP. The number of reattachment sites of the free shear layer reduces as the RRP increases, lowering the turbulence level and thus the Nusselt number. As a result, the maximum heat transmission occurs at a relative roughness pitch of 5 and decreases as the RRP increases. Table 4 illustrates the % change in Nusselt number when RRP (P/e) increases.

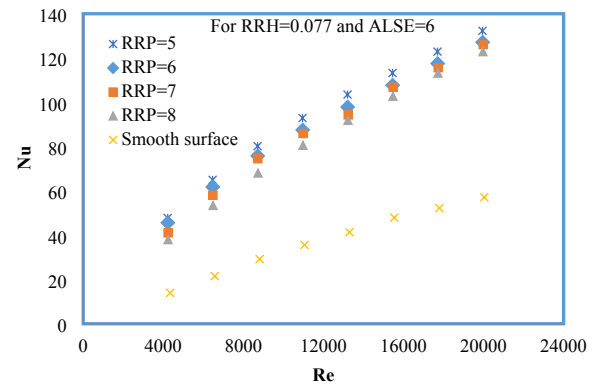


Fig. 6. Changes in Nusselt number (Nu) against Re for various value of RRP and constant values of RRH = 0.077, ALSE = 6.

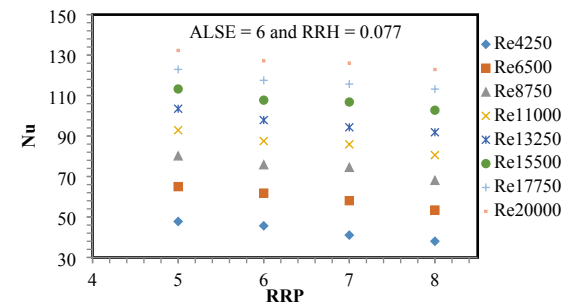


Fig. 7. Changes in Nusselt number against RRP for various value of Re and constant values of RRH=0.077 and ALSE=6.

Table 3

Change in Nusselt number against RRP

Constant roughness parameters	Change in RRP	Change in Nusselt number (Nu) (%)
RRH= 0.088	5-6	-3.90 – (-5.79)
ALSE=8	6-7	-0.84 – (-10.08)
	7-8	-2.14 – (-8.62)

4.1.3 Effect of Square element size

Fig. 8 shows the changes in Nusselt number as a function of Reynolds number for various arm length sizes with constant values of RRP and RRH. For fixed square element size, it can be seen that the Nusselt number rises as the Reynolds number rises. The Nusselt number rises in tandem with the square element size. It's also worth noting that at ALSE = 10, the Nusselt number is at its

highest.

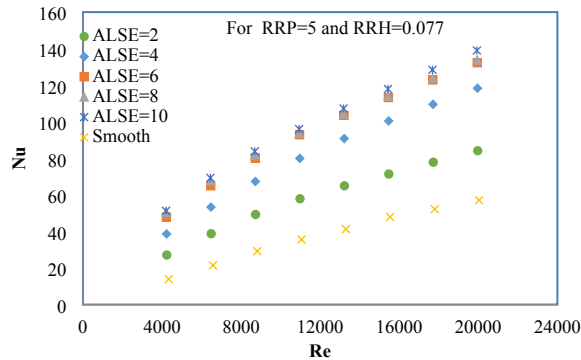


Fig. 8. Change in Nusselt number (Nu) against Reynolds number (Re) for various value of ALSE (A) and constant values of RRP = 5 and RRH = 0.077.

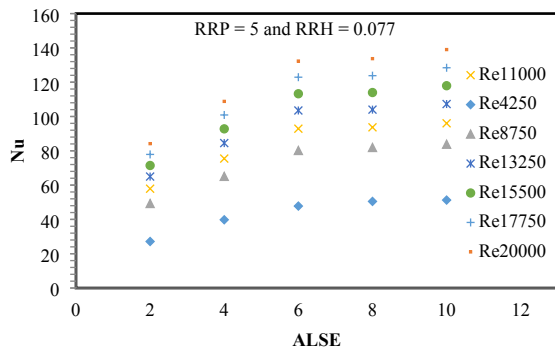


Fig. 9. Changes in Nusselt number (Nu) against ALSE (A) for various values of Reynolds number (Re) and constant values of P/e = 7 and e/D = 0.088.

Table 4

Changes in Nusselt number against ALSE (A)

Constant roughness parameters	Change in ALSE (A)	Change in Nusselt number (Nu) (%)
RRH = 0.077	4-6	20.05 – 23.20
RRP = 5	6-8	0.49 – 5.69
	8-10	1.55 – 3.95

Fig. 9 was created using the data in Fig. 8 to look at how the Nusselt number changes as the ALSE (A) grows for different Reynolds numbers while keeping the other parameters constant. It is noticed that the Nusselt number increases as the ALSE (A) increases, with the highest Nusselt number corresponding to a square element size of 10. Table 4 shows the % change in Nusselt number as square element size increases (A).

4.1.4 Change in Nusselt number against

Reynolds number for the whole range of trials

Fig. 10 depicts the Nusselt number's variation with regard to Reynolds number for all sets of the studies. For the whole range of trials, the Nusselt number rises as the Reynolds number rises. The highest Nusselt number 139 is found at RRP = 5, RRH = 0.077, and ALSE = 10.

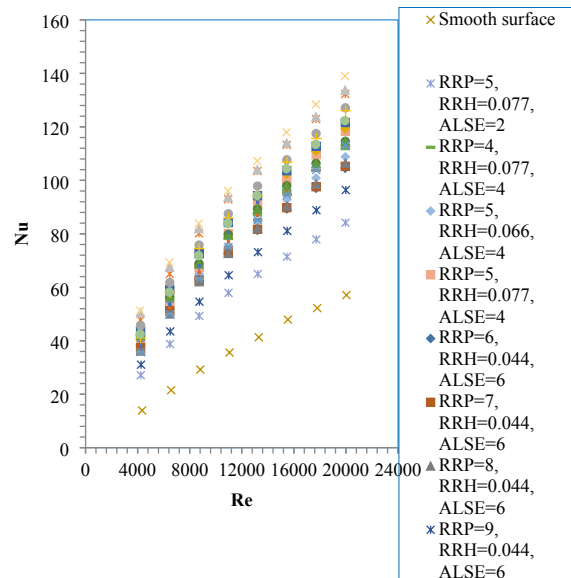


Fig.10. Changes in Nusselt number (Nu) against Re for all set of experiment.

4.2 Characteristics of Friction factor

Artificial roughness improves both the rate of heat transmission and the penalty of blowing air through the duct, i.e. the friction factor. Diagonally chamfered square elements used as roughness arranged in different fashion has been investigated in preset study and found significant impact on friction factor which is discussed as follows.

4.2.1 Effect of Relative Roughness Height (RRH)

For constant values of RRP (P/e) and ALSE (A), the change in friction factor against Reynolds number for different values of RRH (e/D) is shown in Fig. 11. It can be shown that when the Reynolds number rises, the friction factor decreases.

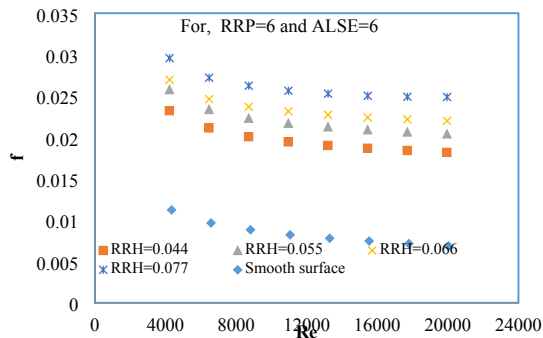


Fig. 11. Changes in friction factor (f) against Re for various value of RRH and constant values of RRP=6 and ALSE=6.

Fig. 12 was generated from the data in Fig. 11 to demonstrate the influence of RRH on friction factor. The friction factor increases as the relative RRH increases, peaking at 0.077. Table 6 shows the percentage change in Friction factor as RRH rises.

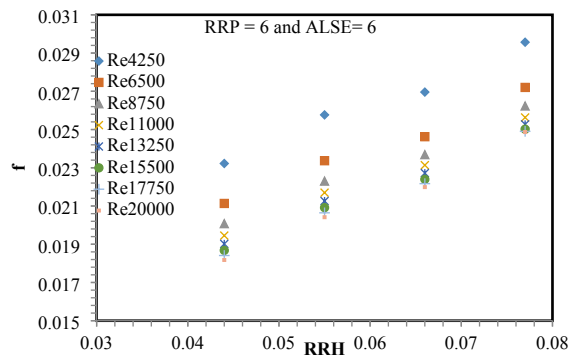


Fig.12. Changes in friction factor (f) against RRH for various value of Reynolds number (Re) and constant values of RRP = 6 and ALSE = 6.

Table 5

Changes in friction factor against RRH		
Constant roughness parameters	Change in RRH (e/D)	Range of variation of Friction factor (f) (%)
	0.044-0.055	10.58-12.30
RRP = 6,	0.055-0.066	4.63-7.71
ALSE = 6	0.066-0.077	9.68-13.10

4.2.2 Effect of Relative Roughness Pitch

Fig.13 shows the fluctuation of Friction factor (f) when Reynolds number (Re) increases for various values of RRP with a

fixed value of RRH = 0.077 and ALSE = 6. The plot shows that at a certain value of RRP, Friction factor (f) falls as Reynolds number increases. Because there is less impediment on the flow route, Friction factor (f) lowers when Relative roughness pitch (P/e) increases. It can also be noticed that for all sets of relative roughness height and arm length size of square elements, the maximum in Friction factor correspond to the minimum Relative roughness pitch.

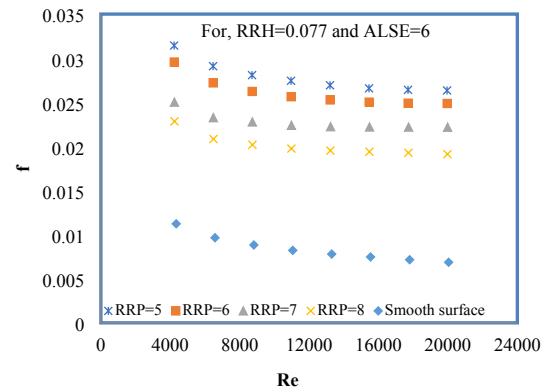


Fig. 13. Changes in friction factor (f) against Re for various value of RRP and a constant value of RRH = 0.077 and ALSE = 6.

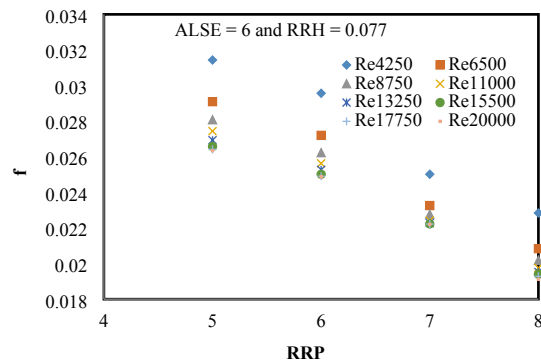


Fig. 14. Changes in friction factor (f) against RRP for different values of Re and a fixed value of RRH = 0.088 and ALSE = 6.

Fig. 14 was generated using the data in Fig. 13 to demonstrate the influence of relative roughness pitch on friction factor. Fig. 14 demonstrates that when the relative roughness pitch (P/e) grows, the friction factor declines, with the highest value of friction factor corresponding to P/e of 5, A of 6, and e/D of 0.077. The distance between the roughness components grows as the relative roughness pitch grows, resulting in reduced obstruction to

air movement and a lower friction factor. Table 7 illustrates the % change in friction factor when P/e increases.

Table 6

Changes in friction factor against RRP		
Fixed roughness parameters	Change in RRP (P/e)	Range of variation of Friction factor (f) (%)
RRH= 0.088	5-6	(-5.60) - (-6.60)
ALSE=8	6-7	(-10.71) - (-15.39)
	7-8	(-8.70) - (-13.90)

4.2.3 Effect of Arm length of square element (ALSE)

Fig.15 shows the change in friction factor (f) as a function of Reynolds number for various square element sizes with constant relative roughness pitch of 5 and relative roughness height of 0.077. The Friction factor grows as the square element size increases, as can be observed.

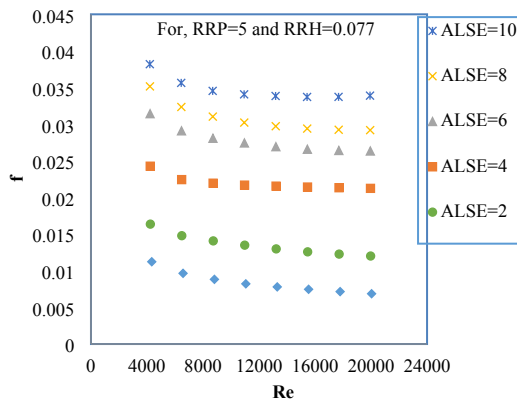


Fig. 15. Changes in friction factor (f) against Re for various values of ALSE and constant values of RRP=5 and RRH=0.077.

Fig. 16 shows that the Friction factor (f) grows as ALSE (A) increases. Table 7 shows the percentage change in Friction factor as the ALSE (A) grows.

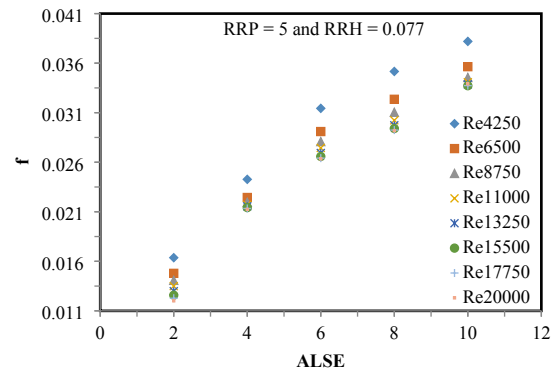


Fig. 16. Changes in friction factor (f) against ALSE (A) for various value of Reynolds number (Re) and a fixed value of RRP = 5 and RRH = 0.077.

Table 7

Constant roughness parameters	Change in ALSE(A)	Variation of friction factor (f) (%)
RRH = 0.077	4-6	23.99-29.52
RRP = 5	6-8	10.80-11.85
	8-10	8.62-16.14

4.2.4 Variation of Friction factor as a function of Reynolds number

For all sets of data, Fig.17 depicts the fluctuation of Friction factor (f) as a function of Reynolds number. For full sets of data, the Friction factor (f) falls as the Reynolds number rises. The friction factor also increases when the values of RRH, RRP, and ALSE increase. At RRP of 5, RRH of 0.055, and ALSE of 10, the greatest Friction factor discovered is 0.03819, which corresponds to Reynolds number of 4250.

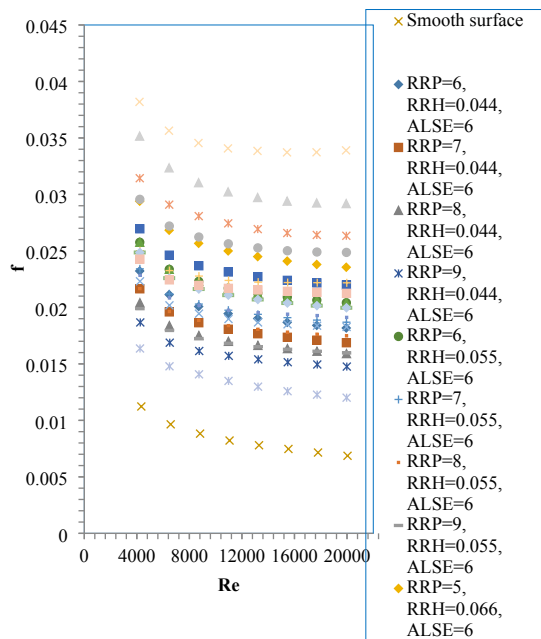


Fig. 17. Change in friction factor (f) against Reynolds number (Re) for all set of experiments.

4.3 Enhancement of Heat Transfer And Friction Factor

The Nusselt number enhancement ratio is used to compare the heat transfer enhancement of a roughened duct with chamfered square element to that of a smooth duct. The Nusselt number enhancement ratio is defined as the ratio of the roughened duct Nusselt number to the smooth duct Nusselt number [17] at similar flow circumstances and can be explained as follows:

$$\text{Enhancement ratio} = \frac{Nu_r}{Nu_s} \quad (10)$$

For various roughness geometry parameters, Fig.18 depicts the fluctuation of Enhancement ratio (Nu_r / Nu_s) as a function of Reynolds number.

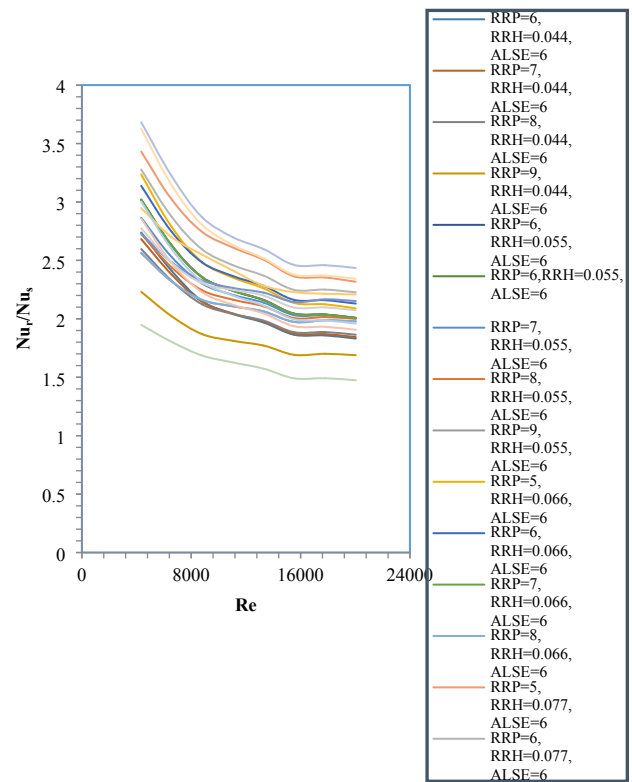


Fig. 18. Changes in enhancement ratio (Nu_r/Nu_s) against Re for entire set of experiment.

The use of a chamfered square element as an artificial roughness over the absorber plate of a SAH improves the heat transfer rate while increasing the friction factor. The ratio of the friction factor achieved by the roughened absorber plate to that obtained by the smooth absorber plate [17] at similar flow circumstances may be determined to explain the raise in friction factor.

$$\text{Friction factor ratio} = \frac{f_r}{f_s} \quad (11)$$

The fluctuation of the Friction factor ratio (f_r/f_s) against Reynolds number is depicted in Fig. 19.

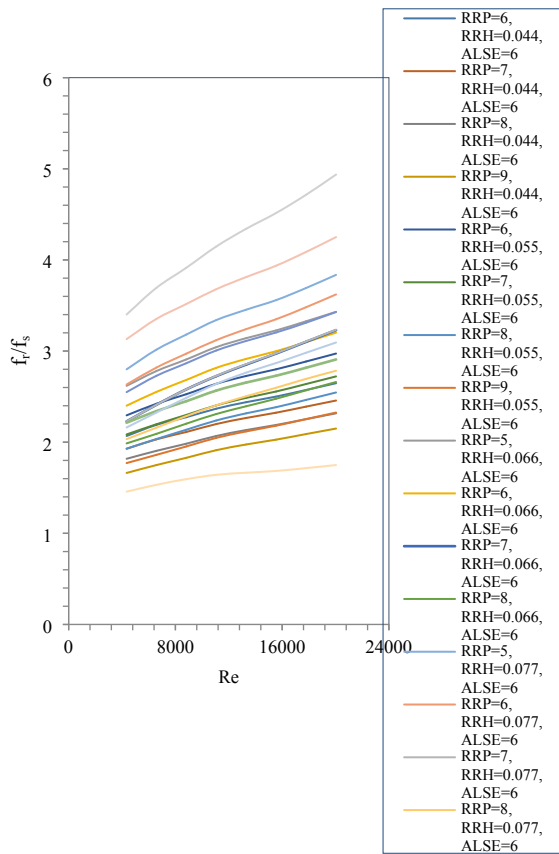


Fig. 19. Changes in friction factor ratio (f_r/f_s) against Re for entire set of tests.

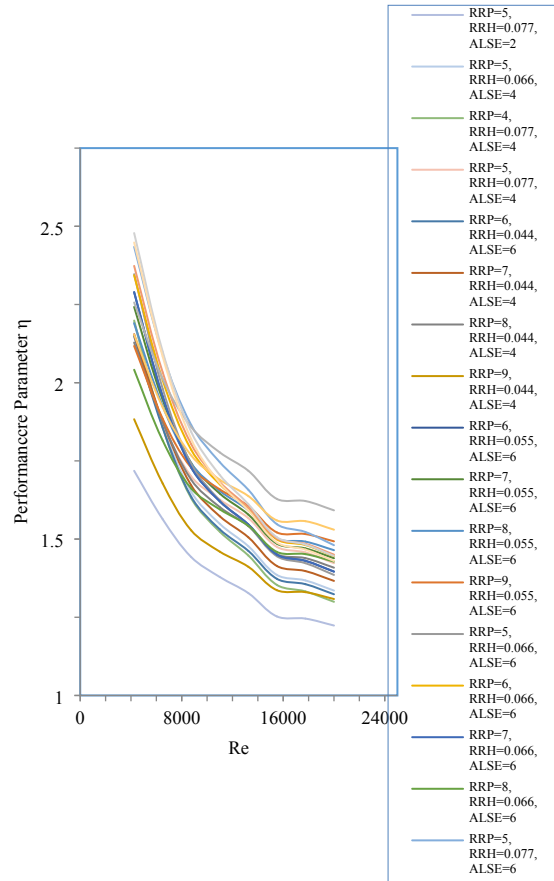


Fig. 20. Deviation of Performance parameter (η) with Re for entire set of tests.

4.4 Performance Parameter

The use of artificially roughened surfaces on the absorber plate of a SAH raises the Nusselt number while also raising the friction factor. The pumping force required to blow the air through the duct increases as the friction factor rises. To get the most out of the roughened absorber plate, the Nusselt number should be as high as feasible while the friction penalty is kept as low as possible. As a result, a performance parameter is examined and defined in order to forecast the total performance of the solar air heater [18].

$$\text{Performance parameter, } \eta = \frac{Nu_r}{\left(\frac{f_r}{f_s}\right)^{\frac{1}{3}}} \quad (12)$$

Fig. 20 depicts the fluctuation of the performance parameter with respect to Reynolds number for all of the roughness geometries tested. The higher the value of the performance parameter is above unity, the better the solar air heater's performance. It's also worth noting that the value of the performance parameter is greater than unity for the whole range of Reynolds numbers. Furthermore, the value of the performance parameter is highest at Re of 4250 for all forms of roughness geometry. Following that, it significantly drops up to Re of 8250, after which it becomes asymptotic for higher Reynolds numbers.

Temperature distribution at different location of SAH may be seen in Fig. 21 and Fig. 22. The temperature distribution of the absorber plate is depicted in Fig. 21, where it can be observed that heat transfer reduces along the flow as the heat capacity of air

falls as the difference in temperature between the absorber surface and the blowing air diminishes. It may see in the Fig. 22 that the air temperature increases along the flow.

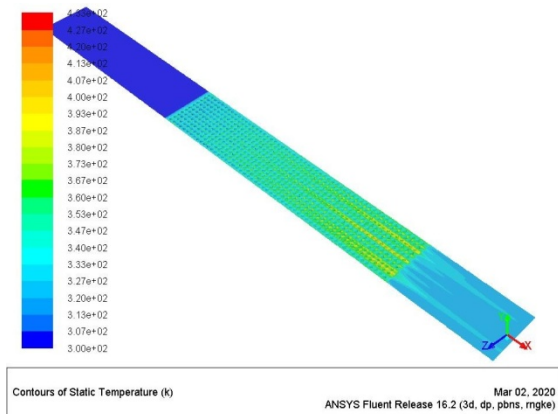


Fig. 21. Temperature distributions over absorber plate and top surface.

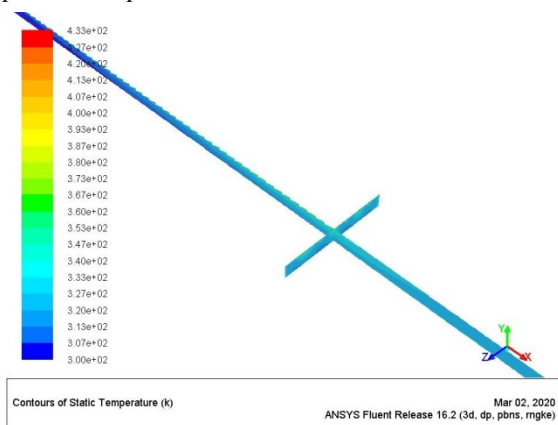


Fig. 22. Temperature distributions on mid of roughened absorber plate normal to stream-wise direction and on a roughness row along direction of flow.

5. Methodology for Correlation Development

The correlations for Nusselt number and friction factor are produced in this section using Microsoft Excel software to do regression analysis using the approach proposed by Saini and Saini[20]. During the regression analysis, data was plotted on a log-log scale in order to achieve the optimum curve fitting. Data regression is discovered to deal with the first order. When two variables

are equal, the relationship is the simplest. When one variable is equal to the other multiplied by a constant, the connection is the next simplest. The relationship is said to be linear in either instance. A linear connection, often known as a straight line, has a single variable with the highest power of one, and is written as:

$$y = mx + c \tag{13}$$

Where m is the line's slope and c is the line's intercept or ordinate. By changing the value of x and y into its logarithmic value, the first order equation for a straight line can be written as:

$$\log y = m \log x + c_1 \tag{14}$$

Or

$$\log y = \log x^m + \log (\text{anti log } c_1) \tag{15}$$

Or

$$\log y = \log [(\text{anti log } c_1) (x^m)] \tag{16}$$

The above equation can be expressed as follows by using antilog on both sides:

$$y = (\text{anti log } c_1) (x^m) \tag{17}$$

This is the most common type of first-order equation. The first order regression of the data on a plot of $\log x$ and $\log y$ yields the values of c_1 and m . Equation (17) can be used to obtain the first order equation by plugging in the values of c_1 and m .

It can be seen that $\ln(Y)$ and $\ln(Z)$ have a polynomial functional connection of the kind shown below (A). For first order equation for a polynomial functional relationship can be written as [15]:

$$\ln(Y) = \ln(m_1) + m_2 \ln(A) + m_3 \{\ln(A)\}^2 \tag{18}$$

For each plot, the coefficients m_1 , m_2 , and m_3 were obtained, and it was discovered that the coefficients m_2 and m_3 are almost identical for all plots, although m_1 varied. The average values of m_1 , m_2 , and m_3 were calculated, and the equation was then rearranged as follows:

$$Y = m_4 A^{m_2} \exp \{m_3 \ln(A)\}^2 \tag{19}$$

Where m_4 is anti $\ln(m_1)$

The Nusselt number and friction factor, as determined by the results, are completely

reliant on roughness parameters and flow parameters, notably RRH (e/D), RRP (P/e), ALSE (A), and Reynolds number (Re). As a result, the following functional equation can be used to represent the Nusselt number and friction factor:

$$Nu = Nu(Re, P/e, A/6, e/D) \quad (20)$$

$$f = f(Re, P/e, A/6, e/D) \quad (21)$$

5.1 Correlation development for Nusselt number

The functional correlations between the Nusselt number and other roughness parameters as well as the Reynolds number have already been examined. Nusselt number rises as Reynolds number rises, and the power law governs the functional relationship between the two, as detailed in Section 7 on methodology. For all 184 simulation data obtained from ANSYS Fluent for all 23 artificially roughened absorber plates tested, a regression analysis was used to create statistical correlations using Microsoft Excel. As illustrated in Fig. 23, the values of $\ln(Nu)$ are shown as a function of $\ln(Re)$. The following is the best-fitting equation for Nusselt number discovered by regression analysis:

$$Nu = A_0 Re^{0.67} \quad (22)$$

The coefficient A_0 is affected by the remaining factors, such as P/e , $(A/6)$ and e/D . Now, as shown in Fig. 24, the value of $Nu/Re^{0.67} = (A_0)$ against all values of P/e is displayed on a log-log scale to determine the effect of relative roughness pitch on Nusselt number. A second order polynomial is fitted through these points on a log-log scale using regression analysis, and it looks like this:

$$Nu = B_0 Re^{0.67} (P/e)^{1.17} \exp(-0.386(\ln(P/e))^2) \quad (23)$$

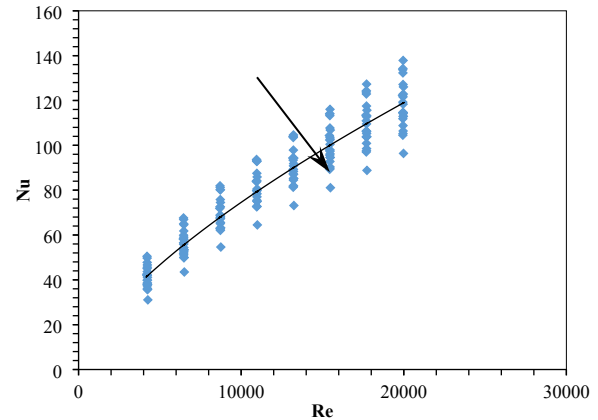


Fig. 23. Nu as a function of Re.

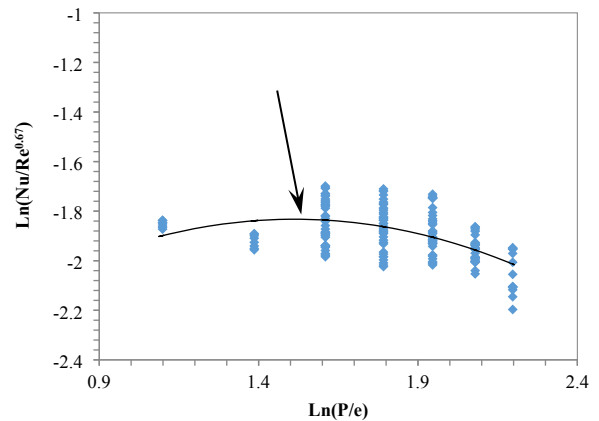


Fig. 24. $\ln(Nu/Re^{0.67})$ as function of $\ln(P/e)$.

In fact, the coefficient B_0 will depend on the remaining roughness parameters e/D and $(A/6)$. Taking the parameter ALSE of $(A/6)$ into account, the value of $Nu/Re^{0.67} (P/e)^{1.17} \exp(-0.386(\ln(P/e))^2) = (B_0)$ corresponding to all values of $(A/6)$ is displayed on a log-log scale in Fig. 25. Now we use regression analysis to fit a second order polynomial through these locations, as follows:

$$Nu = C_0 Re^{0.67} (P/e)^{1.17} \exp(-0.386(\ln(P/e))^2) (A/6)^{0.33} \exp(0.506(\ln(A/6))^2) \quad (24)$$

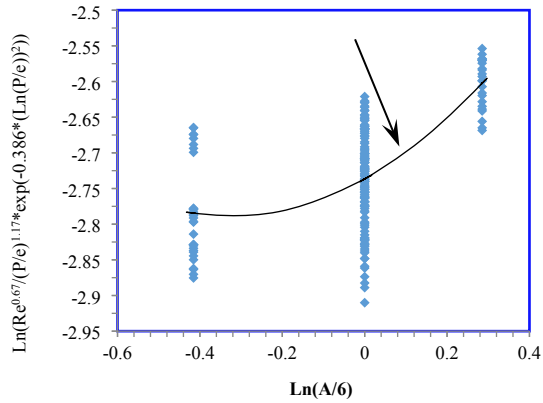


Fig. 25. $\ln(\text{Nu}/\text{Re}^{0.67}/((P/e)^{1.17} \exp(-0.386 (\ln(P/e))^2)))$ as function of $\ln(A/6)$.

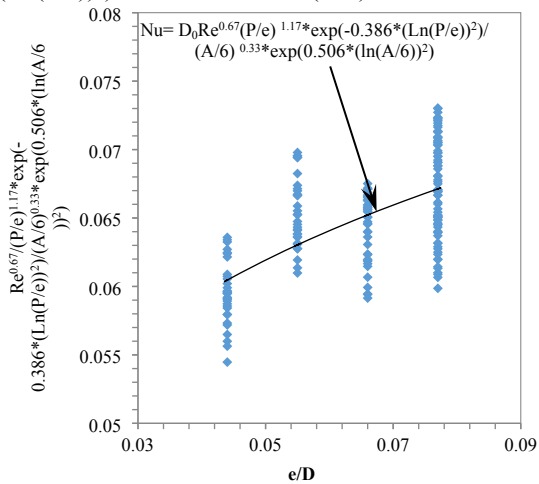


Fig. 26. $\text{Nu} / \text{Re}^{0.67}/(P/e)^{1.17} \exp(-0.386 (\ln(P/e))^2) / (A/6)^{0.33} \exp(0.506 (\ln(A/6))^2)$ as function of e/D .

In fact, the coefficient C_0 will be a function of the other roughness parameter e/D . Considering RRH (e/D) into account, the value of $\text{Nu}/\text{Re}^{0.67}/(P/e)^{1.17} \exp(-0.386 (\ln(P/e))^2) / (A/6)^{0.33} \exp(0.506 (\ln(A/6))^2) = C_0$ against all values of (e/D) is shown on a log-log scale in Fig. 26. According to the regression analysis, the fittest equation for Nusselt number is as follows:

$$\text{Nu} = D_0 \text{Re}^{0.67} (P/e)^{1.17} \exp(-0.386 (\ln(P/e))^2) / (A/6)^{0.33} \exp(0.506 (\ln(A/6))^2) (e/D)^{0.19} \quad (25)$$

The value of D_0 , which offers the final form of correlation for Nusselt number, is determined via regression analysis to best fit a straight line through these points.

$$\text{Nu} = 0.108 \text{Re}^{0.67} \left(\frac{P}{e}\right)^{1.17} \left(\frac{e}{D}\right)^{0.19} \left(\frac{A}{6}\right)^{0.33} \left[\exp\left\{-0.386 \left(\ln\left(\frac{P}{e}\right)\right)^2\right\}\right]$$

$$\left[\exp\left\{0.506 \left(\ln\left(\frac{A}{6}\right)\right)^2\right\}\right] \quad (26)$$

As illustrated in Fig. 27, the projected Nusselt number values from the developed correlation were compared to numerical values at a 95% confidence level. As can be seen, these in Figs are reasonable because the highest variance is less than 9%.

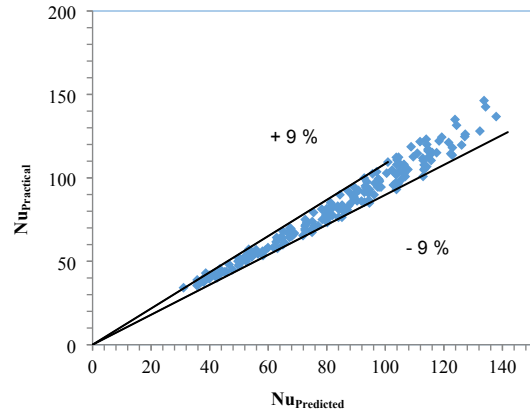


Fig. 27. Comparison for Nusselt Number's predicted and numerical values.

5.2 Correlation development for Friction Factor

The roughness geometry and flow parameters have also been discovered to have a considerable influence on the friction factor. The friction factor reduces as the Reynolds number increases, and the power law governs the functional relationship between the two, as mentioned in section 5 on methodology. For the establishment of a correlation for friction factor, a similar process was used, and the final correlation was as follows:

$$f = 0.087 \text{Re}^{-0.12} \left(\frac{P}{e}\right)^{1.16} \left(\frac{e}{D}\right)^{0.26} \left(\frac{A}{6}\right)^{0.48} \left[\exp\left\{-0.49 \left(\ln\left(\frac{P}{e}\right)\right)^2\right\}\right] \left[\exp\left\{0.706 \left(\ln\left(\frac{A}{6}\right)\right)^2\right\}\right] \quad (27)$$

Fig. 28 shows a comparison of the anticipated Friction factor values from the developed correlation with numerical values at a 95% confidence level. As can be seen, these Figs are reasonable and have a maximum variance of less than 10%.

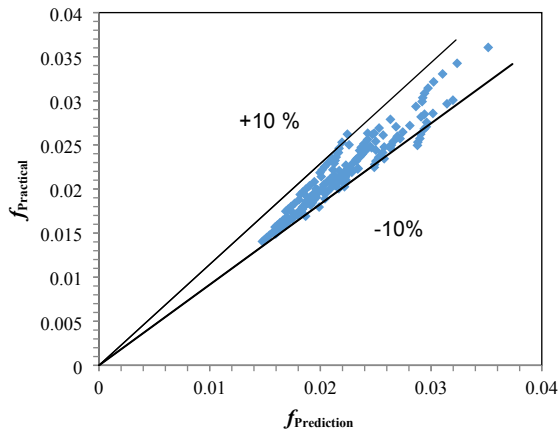


Fig. 28. Comparison for friction factor's predicted and numerical values.

6. Conclusions

The thermohydraulic performance of a SAH having absorber plate roughened by chamfered square roughness elements was investigated using three-dimensional CFD simulations in this paper. The investigation's major findings are as follows:

1. The Nusselt number and friction factor grows as RRH increases for the entire range of Reynolds numbers.
2. Nusselt number and friction factor decrease as relative RRP increases.
3. Nusselt number and friction factor grow as the ALSE (A) increases. The Nusselt number that corresponds to a ALSE of 6 has been shown to be the best.
4. In comparison to a smooth duct, the Nusselt number and friction factor both increase by 3.62 and 3.14 times, respectively.
5. Nusselt number and friction factor correlations have been established for the roughness geometry parameter and flow parameters.
6. When the numerical values of Nusselt number and friction factor predicted by the respective correlation are compared at the 95 percent confidence level, it is found that 174 out of 184 values (96 percent) of the predicted data values lie within 9% and 10% of numerically observed data values, respectively.

References

- [1] Man Singh Azad, Apurba Layek "Performance Analysis of solar air heater having absorber plate artificially roughened by chamfered-square elements" *Journal of Solar Energy Research*, Vol. 4, No. 1 (2019) 73-83 doi: 10.22059/JSER.2019.70908
- [2] Hachemi A. "Thermal performance enhancement of solar air heaters by a fan-blown absorber plate with rectangular fins". *Int. J. Energy Res.* 1995;19:567-577.
- [3] Ibrahim Z, Ibarahim Z, Yatim B, Ruslan H Md. Thermal efficiency of single-pass solar air collector. *AIP Conference Proceedings* 1571, 90 (2013); doi:10.1063/1.4858635.
- [4] Chabane F, Moumimi N, Benramache S. "Experimental study of heat transfer and thermal performance with longitudinal fins of solar air heater". *J. Adv. Res.* 2014;5: 183-192.
- [5] Chabane F, Moumimi N, Benramache S, Bensahal D, Belahssen O. "Collector efficiency by single pass of solar air heaters with and without using fins". *Eng. J.* 2012;17:43-55
- [6] Roy A, Hoque E Md. "Performance analysis of double pass solar air heater with packed bed porous media in Rajshahi". *AIP Conference Proceedings* 1851, 020010 (2017); <https://doi.org/10.1063/1.4984639>.
- [7] Kumar TS, Thakur NS, Kumar A, Mittal V. "Use of artificial roughness to enhance heat transfer in solar air heaters - a review". *J. Energy Southern Africa* 2010;21:35-51
- [8] Dogra S. "Effect of artificial roughness on thermal and thermo-hydraulic efficiency in rectangular duct of a double pass solar air heater by using transverse ribs on the absorber plate". *Int. J. Mod. Eng. Res.* 2013;3: 2271-2274.
- [9] Rajpoot SS, Koli DK. "CFD analysis of solar air heater duct with rectangular rib surface". *Int. J. Eng. Trends Tech.* 2013;4: 3006-3011.
- [10] Vyas AA, Shringi D. "CFD based thermal efficiency analysis of solar air heater with smooth plate and perforated plate". *Imp. J. Interdisc. Res.* 2017;3:415-422.
- [11] Prasad BN, Saini JS. "Effect of artificial roughness on heat transfer and friction factor in a solar air heater". *Solar Energy* 1988;41:555-560.
- [12] Karwa R, Bairwa RD, Jain BP, Karwa N. Experimental study of the effects of rib angle and discretization on heat transfer and friction in an asymmetrically heated rectangular duct. *J. Enhanced Heat Transf.* 2005;12:343-55.
- [13] ArjumandRasool, Adnan Qayoum. Numerical analysis of heat transfer and friction factor in

- two-pass channels with variable rib shapes. International Journal of Heat and Technology. 36 (91) 2018, 40-48. <https://doi.org/10.18280/ijht.360106>
- [14] Tapas V, Sao AK, Sharma P. “Computational analysis of an artificial roughened surface of solar air heater”. Int. J. Innovative Res. Sci. Eng. Tech. 2015;4:12205-12212. DOI:10.15680/IJRSET.2015.0412092
- [15] Man Singh Azad, Apurba Layek “Correlation for Nusselt number and Friction Factor for Solar Air Heater Having Absorber Roughened by Chamfered-square Elements” International Journal of Fluid Mechanics & Thermal Sciences, 2019; 5(2): 50-62, doi: 10.11648/j.ijfmts.20190502.13
- [16] Thakur SK, Mittal V, Thakur NS, Kumar A. Heat transfer and friction factor correlations for rectangular solar air heater duct having 60° inclined continuous discrete rib arrangement. British J. Appl. Sci. Tech. 2011;1:67-93.
- [17] Kumar M, Varun. A computational fluid dynamics investigation of solar air heater duct provided with inclined circular ribs as artificial roughness. Bonfring Int. J. Ind. Eng. Manag. Sci. 2014;4:115-120.
- [18] Arjumand Rasool, Adnan Qayoum. Numerical analysis of heat transfer and friction factor in two-pass channels with variable rib shapes. International Journal of Heat and Technology. 36 (91) 2018, 40-48.
- [19] Kumar M, Varun. A computational fluid dynamics investigation of solar air heater duct provided with inclined circular ribs as artificial roughness. Bonfring Int. J. Ind. Eng. Manag. Sci. 2014;4:115-120.
- [20] Saini R.P., Saini J.S., Heat transfer and friction factor correlations for artificially roughened Ducts with expanded metal mesh as roughness element, International Journal of Heat and Mass Transfer, Vol. 40(4), 973-986, 1997.